Available online at www.sciencedirect.com

jmr&t Journal of Materials Research and Technology

journal homepage: www.elsevier.com/locate/jmrt

Polylactic acid as biobased binder for the production of 3D printing filaments for Ti6Al4V alloy manufacturing via bound metal deposition

Mario Bragaglia [a], *Matteo Mariani* [a], *Claudia Sergi* [b,*], *Fabrizio Sarasini* [b], *Jacopo Tirillò* [b], *Francesca Nanni* [a]

[a] *University of Rome "Tor Vergata", Department of Enterprise Engineering "Mario Lucertini", and INSTM RU Roma-Tor Vergata, via del Politecnico 1, Rome, 00133 Italy*

[b] *University of Rome La Sapienza, Department of Chemical Engineering Materials Environment, and UdR INSTM, Via Eudossiana 18, Rome, 00184 Italy*

ARTICLE INFO

Article history:
Received 31 July 2023
Accepted 21 September 2023
Available online 26 September 2023

Keywords:
Polylactic acid
Biobased binder
Titanium alloy
Bound metal deposition
Additive manufacturing
Debinding and sintering

ABSTRACT

In this paper, a biobased binder mainly composed of polylactic acid (PLA) was developed for the production of Ti6Al4V feedstock suitable for 3D printing via material extrusion. 3D printed samples were debound via solvent and thermal treatments and successfully sintered in reducing atmosphere obtaining dense metallic components. The designed and produced bio-binder is completely eliminated during the debinding processes leading to sintered samples showing a high densification (93–94%), with a microstructure composed of primary alpha phase with segregated beta phase at grain boundaries and having average grain size of 70 μm. 3D printed sintered samples show good mechanical properties (yield strength (σ_y) = 662 MPa, ultimate tensilte strength (UTS) = 743 MPa, elongation at break (ε_{max}) = 12%, hardness = 5.15 GPa) influenced by the sintering parameters and the presence of some degree of micro-porosity in the final structure.

1. Introduction

Titanium and titanium alloys are widespread metals used in engineering, i.e., automotive, aerospace, oil and gas, and biomedical fields where high specific strength and stiffness and excellent corrosion resistance are required [1].

These materials can be 3D printed via powder bed fusion (PBF) techniques, i.e., laser sintering (SLS) and melting (SLM), electron beam melting (EBM), allowing for the production of complex geometries and shapes unattainable with traditional manufacturing techniques [2]. This higher freedom of design enables structures lightweighting techniques such as generative design (GD) and topology optimization (TO) [3,4] and promotes a new commercial approach, i.e., product customization. Nevertheless, PBF techniques are extremely expensive in terms of both investment and operative costs. Moreover, titanium alloys are extremely difficult to 3D print due to the high oxygen reactivity which imposes the use of protective atmospheres, thus making the manufacturing process even more expensive [5].

Nowadays a new 3D printing technology called Bound Metal Deposition (BMD) is gaining more attention as it allows

* Corresponding author.
E-mail address: claudia.sergi@uniroma1.it (C. Sergi).
https://doi.org/10.1016/j.jmrt.2023.09.227

for the 3D printing of parts with complex geometry, low waste materials and design flexibility at very low cost. BMD involves the preparation of a highly metallic powder-loaded filament, where the polymeric matrix is a binder which is then 3D printed with a standard fused filament fabrication (FFF) printer in the desired shape, and the resulting green body is successively post-processed performing debinding and sintering to get a solid metallic part [6]. The investment costs of FFF 3D printers range from 2000 $ up to 15,000 $ [7], while the ones of SLM and EBM can reach 1 M$ [8]. This clearly highlights the economic advantages of BMD especially for all those companies that work with metal injection molding (MIM) and already own debinding and sintering ovens.

Binder jetting (BJ) is another 3D printing technique which exploits debinding and sintering to obtain the solid metal part starting from the 3D printed green body. The printer dispenses small droplets of a liquid binding agent on a powder bed to bond the powders together and form the final 3D structure [9]. This technique has many advantages such as relatively high build rates and large build volume [10], but the investment costs are still higher than FFF ones ranging from 30,000 $ for a basic machine up to 250,000 $ for large-scale and industrial-style printers [11,12].

Among metals manufactured by BMD, even though steels are the most employed [13], there are several research studies dealing with copper [14], titanium and titanium alloys [15–17]. In particular, Thompson et al. [15] focused on pure titanium using sintering temperatures between 1300 and 1400 °C and exposure times between 90 and 300 min achieving a relative density of 94%, while Zhang et al. [17] focused on Ti6Al4V using sintering temperatures ranging from 900 to 1340 °C [17] and reaching densities higher than 90% and mechanical properties close to literature [18,19].

The 3D printing of titanium alloys, and in general of a metal feedstock, is non-trivial since the filler loading must be high, in the range of 55–65 vol. % to obtain dense sintered metals [20]. The metallic particles have to be very close one to each other to allow the sintering process, involving the lattice and grain boundary diffusion mechanisms. Moreover, despite being eliminated during the debinding process, the binder system plays a significant influence on the whole manufacturing process, and it has a strong impact on the quality of the final products [21].

It was shown that the choice of the binder systems is paramount to the quality of filaments, changing from highly flexible to very brittle [22] and as a general trend, the higher the filler content, the more brittle is the resulting filament. This is a critical point, as the filament must show enough stiffness and strength to be easily spooled, unspooled and extruded through the nozzle during the FFF printing. The filament must show also a good melt rheology, in order to be deposited as layer by layer structure, and generally the higher the filler loading the higher the melt viscosity and the lower the processability [23]. Melt viscosity indeed depends on the solid loading, the binder rheology, the printing temperature, the state of agglomeration and the shear rate generated during extrusion [24]. Moreover, it depends on the particle size [25] as it has been shown that filaments made of particles having high average size (>50 μm) displayed less printability due to high viscosity [26,27].

Typically, the binder system is made of: i) a backbone binder, which is the component that holds the shape, ii) a second polymeric phase which is generally a mix of polymers and waxes and guarantees good rheological behavior, and iii) other additives like stabilizers, compatibilizers, and dispersing agents, e.g., stearic acid, which help enhancing the homogenization between powder and binder, avoiding agglomeration and phase separation [21,28,29]. The binder system is typically removed by solvent, catalytic [29,30] and thermal debinding [21,31] or a combination of the previous ones depending on its composition. The binder must be entirely removed before the final step of sintering, as an incomplete binder removal will lead to the formation of defects that affect the quality of sintered parts [29]. Incomplete binder removal due to incorrect debinding temperature, excessively high heating rate, insufficient holding time, and debinding atmosphere [21] determines the arising of defects, i.e., porosity, cracks, blistering, bloating [32], carbon product formation, generally caused by the fast decomposition of the binder components.

Synthetic polymers such as polyolefins, i.e., polyethylene, polypropylene, are generally employed as backbone binders for BMD of titanium [33]. But in the last years always more attention is paid to sustainability and in this perspective the use of biopolymers as backbone binder could lead to a more sustainable process. This work originates from the idea that an ecofriendly binder with a biobased backbone polymer could be employed for the FFF manufacturing of titanium parts.

Polylactic acid (PLA) is a biobased semi-crystalline aliphatic polymer, derived from sugarcane corn starch, and cassava roots and belonging to the polyester family [34]. It is one of the most widely used biopolymers and considering its low melting viscosity and its propensity to be loaded with high filler content [35], it results to be the ideal candidate as backbone polymer for the binder. Its origin from renewable resources allows to decrease significantly the fossil fuel and resources use [36].

Debinding process is generally followed by sintering process, which is performed at 0.7–0.9 of the melting temperature, to consolidate particles forming coherent bonds with consequent densification and shrinkage. Sintering temperature and time are the most significant process parameters along with heating and cooling rate, sintering atmosphere [32]. High sintering temperature and sintering time lead to a general decrease of the porosity and enhancement of the density, but induce also the increase in the grain size thus influencing mechanical properties such as hardness and strength [5]. Not optimized debinding and sintering processes produce components presenting microstructural defects and porosity and low resulting mechanical properties [37]. This aspect is crucial for all hybrid methods, i.e., MIM, BJ and BMD, which have to convert a green part in a solid metallic one, but it is even more critical for BMD and BJ where an inaccurate printing may result in a higher porosity of the original green part. In any case, a good packing of the powder bed in BJ, i.e., 70% [38], and an optimization of the printing parameters, i.e., flow rate, layer thickness, extrusion temperature, printing speed, in BMD [39] allow to level off this issue ensuring mechanical properties perfectly comparable with MIM ones.

Table 1 – Binder composition.

Binder component	wt.%
PLA	55
EPDM	20
EVA	5
PW	15
SA	5

In this work, in view of a low environmental impact process, a feedstock made of biobased PLA binder highly loaded with Ti6Al4V particles has been extruded in filaments which have been 3D printed via a low-cost FFF technique and successively sintered to obtain metallic parts. The 3D printed parts were thermally treated in order to remove the binder and achieve the sintering. The resulting metallic parts were characterized performing morphological, microstructural, and mechanical tests. The exploitation of a biobased polymer for the production of the Ti6Al4V-filled filament, with a view to decreasing the environmental impact of the overall manufacturing process, and the successful exploitation of this feedstock for the manufacturing of performing metallic component is the main merit of the present work compared to previous works which used petroleum-based feedstocks.

2. Materials and methods

2.1. Materials used and their characteristics

The designed and developed feedstock is composed of spherical gas atomized Ti6Al4V powder supplied by EOS (Titanium Ti64, *EOS GmbH, Hamburg, Germany*) as metallic filler, while the organic binder composition is reported in Table 1. Polylactic acid (PLA, *3052D*, supplied by *Nature Works®* with a molecular weight Mn = ca. 6×10^4 g/mol) was used as backbone binder, ethylene polypropylene diene monomer (EPDM, *Dutral 4047 Eni Versalis*), ethylene vinyl acetate (EVA, *Powder EVA ML 20, Arcoplex Group*) and paraffin wax (PW, *Sigma Aldrich, St. Louis, Missouri, USA*) were used as secondary binders, while stearic acid (SA, *Sigma Aldrich, St. Louis, Missouri, USA*) was used as compatibilizer.

The feedstock formulation was designed starting from the main guidelines for Metal Injection Molding (MIM) binder formulation [40]. Indeed, the binder is made of at least two binder components. The first component, i.e., the primary binder, is easily removable at a low temperature during solvent debinding opening up a pore network through which the second binder, i.e., the backbone, can escape during thermal debinding. Paraffin wax and PLA were selected as primary binder and as backbone in the present work, respectively. Stearic acid was added to enable a good wettability of powders surface with the binder and to create a bond between the two major binder components. Moreover, EPDM and EVA were added to increase the flexibility of the filament to make it easily 3D printable via FFF. These components were removed with the primary binder or during thermal debinding along with the backbone binder.

Preliminary characterizations have been performed on raw materials. The titanium powder was characterized by X-ray diffraction (XRD, *Philips X'Pert PRO, Amsterdam, Netherlands*). XRD patterns were acquired in the 2θ range 30–90° in the following conditions: Cu Kα radiation (λ = 1.5408 Å), 40 kV and 40 mA, step size = 0.02°, time per step = 2 s. The morphology of the Ti6Al4V particles was analyzed by a field emission scanning electron microscope (FESEM, MIRA3, Tescan, Brno, Czech Republic) coupled with energy dispersive spectroscopy (EDS, Octane Elect EDAX, Leicester, UK). The particle size distribution was evaluated via image analysis by measuring 1200 different diameters.

2.2. Feedstock development and rheological characterization

The feedstock formulation used in this research was composed of 55 %v/v of Titanium powder and 45 %v/v of binder. The feedstock was compounded in a closed chamber batch mixer (*Brabender GmbH & Co. KG, Duisburg, Germany*) at a temperature of 180 °C for 30 min imposing a rotating speed of 20 rpm. After compounding, the feedstock has been mechanically ground (3 mm) and dried in oven (*Binder E28, Binder GmbH, Tuttlingen Germany*) at 50 °C for 24 h. Rheological test (*RPA 2000, Alpha Technologies, Hudson, USA*), consisting on viscosity measurements in temperature sweep configuration

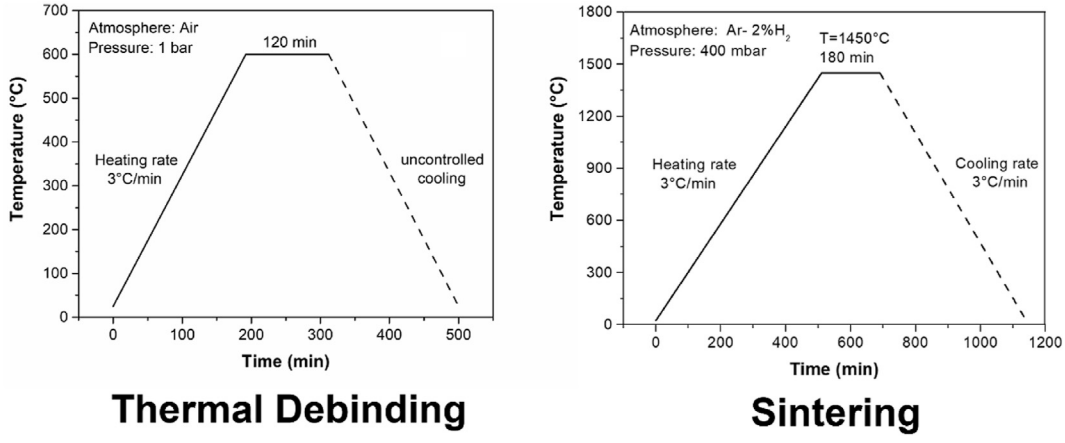

Fig. 1 – Thermal cycles of debinding in air and sintering in a Ar–H_2 atmosphere.

in the range 110–230 °C at a frequency of 1 Hz using a cone–cone geometry, was performed on feedstock.

2.3. Extrusion of filaments and 3D printing

Filaments of feedstock were produced in a single screw extruder (*FILABOT EX2, Filabot, Barre, USA*) with a nozzle diameter of 1.75 mm. Filaments were extruded at a temperature of 180 °C, setting a screw speed of 15 rpm, and coiled in spools. Parallelepipeds having dimensions 30 × 20 × 3 mm and Type V tensile test specimens (having dimension 63.5 × 3.18 × 3.5 mm according to ASTM D638 [41]) have been 3D printed by the FFF (*Apium P155, Apium Additive technologies GmbH, Karlsruhe, Germany*) machine. Moreover, as proof of concept, a ribbed scaffolding base plate was also 3D printed (Fig. 4b). This component having overall dimensions of 45 × 35 mm, height of 30 mm and 5 and 10 mm in diameter through-holes can support the load of scaffold tubes. Slicing was performed using the software *Simplify 3D* and setting the printing parameters summarized in Table 2.

Polyvinylpyrrolidone based fixative for 3D printing (*Dimafix*) was applied to the glass bed for improving the adhesion of first layer. Both filaments and 3D printed samples have been stored in a vacuum desiccator prior to further use.

2.4. Solvent debinding, thermal debinding and sintering

Solvent debinding was performed immersing the 3D printed samples in diethyl ether (*Sigma Aldrich, St. Louis, Missouri, USA*) under magnetic stirring at room temperature for 24 h.

Thermal debinding of previously solvent debound 3D printed samples was performed in a muffle furnace (*Forni De Marco, Rome, Italy*) operating in air atmosphere at 600 °C for 120 min with an heating rate of 3 °C/min and uncontrolled cooling. Sintering was performed at 1450 °C for 180 min in a tubular furnace (*Zsinter, Nanoe, Ballainvilliers, Bretagne, France*) operating in vacuum (400 mbar) and reducing atmosphere of Argon–2% Hydrogen fluxed gas (0.1 L/min) imposing a heating rate of 3 °C/min. Cooling was conducted in the same atmosphere with a cooling rate of 3 °C/min. The debinding and the sintering cycles are reported in Fig. 1. Fig. 2 shows an overview of the overall manufacturing process from the feedstock compounding to the final sintering of the metallic component.

2.5. 3D printed, green and brown parts characterizations

3D printed samples were investigated by Fourier transform infrared spectroscopy (FT-IR). FT-IR analysis (*Agilent Cary 630 FTIR Instrument, Santa Clara, California, USA*) was carried out acquiring spectra in the range 4000–600 cm^{-1}, with 4 cm^{-1} resolution and each spectrum averaged over 32 scans.

Differential scanning calorimetry (DSC) (*Netzsch DSC 214 Polyma, Selb, Germany*) was performed on the binder using samples of 5 mg tested in the temperature range −50 °C-200 °C, in nitrogen atmosphere (40 ml/min) and using heating and cooling rate of 10 °C/min. Thermogravimetric Analysis (TGA) (*PerkinElmer Pyris 1 TGA, Waltham, Massachusetts, USA*) was performed on the 3D printed samples, before and after chemical debinding, to estimate the temperature range of the thermal debinding and to assess the correct removal of the primary binder. The TGA was performed on 5 mg of sample in nitrogen atmosphere (40 ml/min) in the temperature range 25 °C-800 °C with a heating rate of 10 °C/min.

2.6. Sintered 3D printed parts characterizations

Density measurements were carried out according to ASTM D792 [42], using a buoyancy method-based pycnometer (*Sartorius, Göttingen, Germany*) allowing for the determination

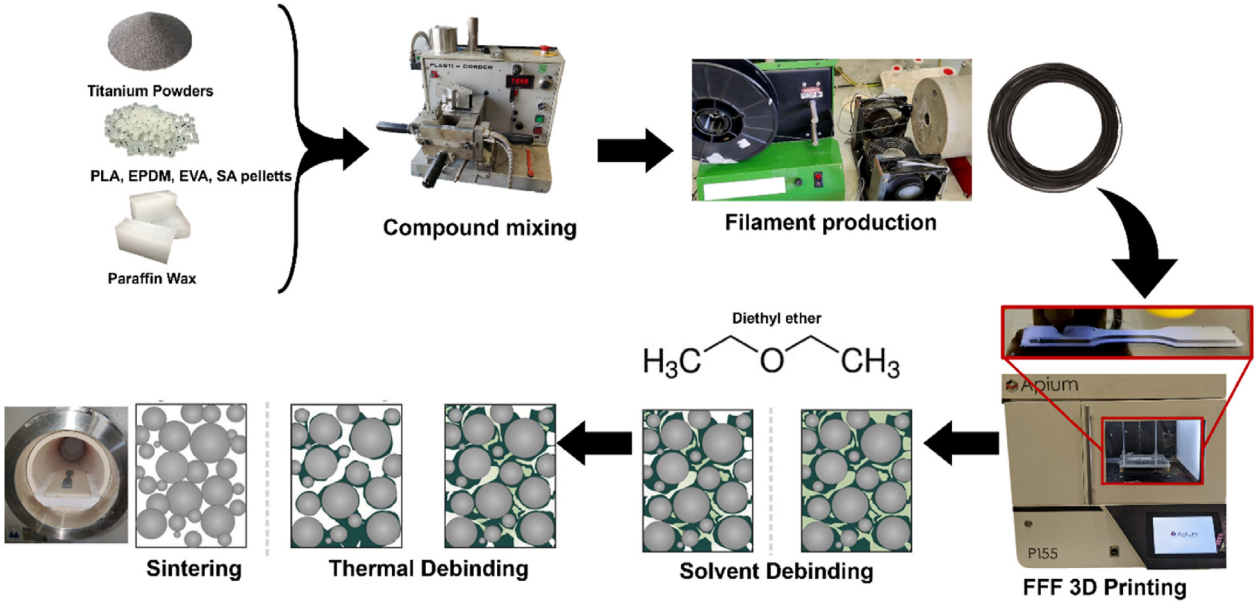

Fig. 2 – Schematization of the overall manufacturing process, i.e., raw materials compounding for feedstock production, filament production through extrusion, FFF 3D printing of specimens and prototypes, solvent and thermal debinding and consolidation through sintering to obtain the final metallic component.

of density by applying Archimedes' Principle. Mean density values were taken from at least three measurements. The crystalline phase analysis of 3D printed sintered samples was performed via XRD (XRD, *Philips X'Pert PRO, Amsterdam, Netherlands*) in the 2θ range 30–90° in the following conditions: Cu Kα radiation (λ = 1.5408 Å), 40 kV and 40 mA, step size = 0.02°, time per step = 2 s.

Sintered 3D printed samples have been cut using a diamond saw (*Buehler Isomet 4000, Buehler, Lake Bluff, Illinois, USA*), and were mounted in epoxy resin (*Epoglass*, curing time of 3 h

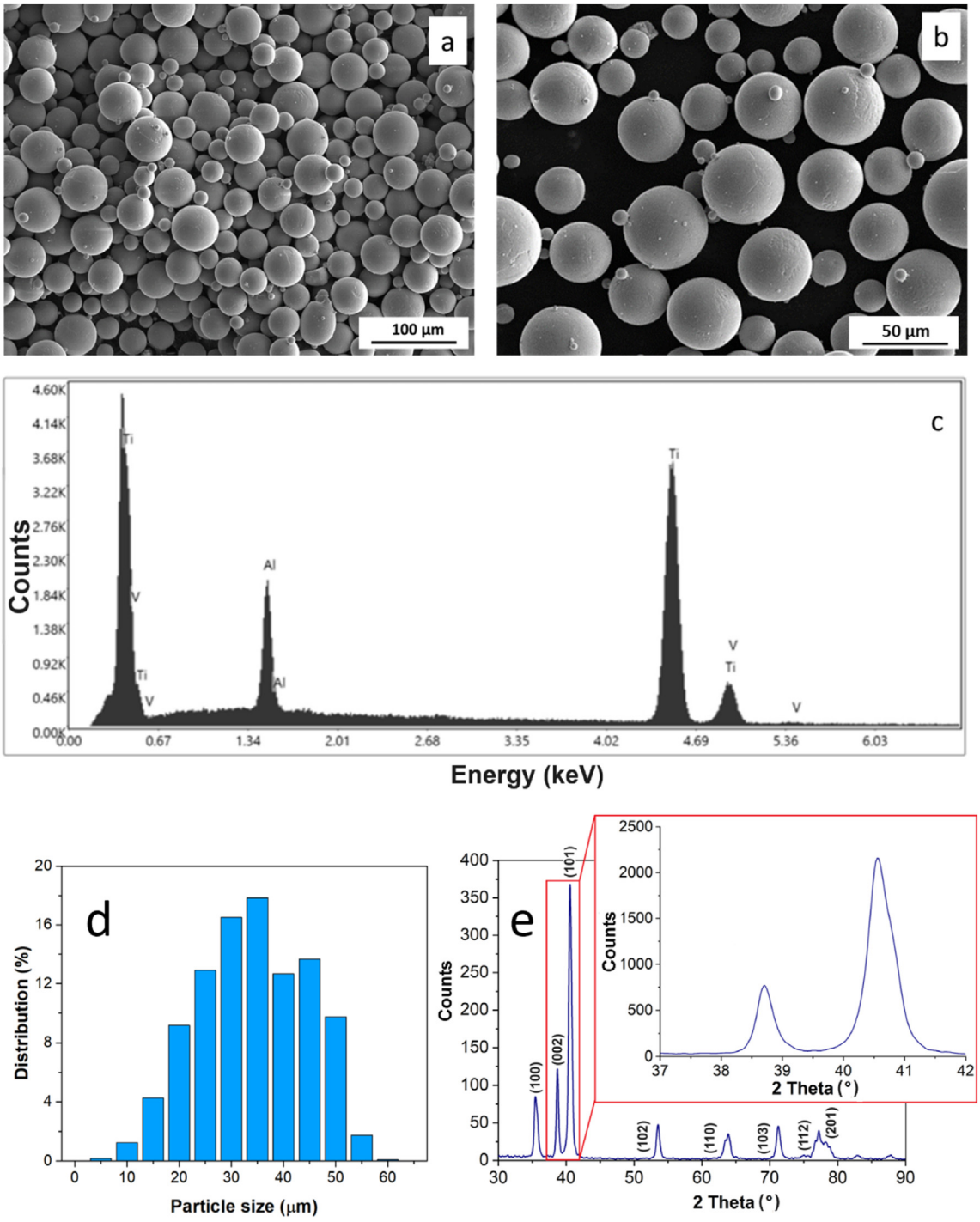

Fig. 3 – SEM micrographs of Ti6Al4V powder at low (a) and high (b) magnification, (c) EDS analysis of the Ti6Al4V particles obtained from SEM micrograph in (a), (d) particle size distribution and (e) XRD pattern of the Ti6Al4V powder in the 2θ range 30–90° with an inset evaluated in the range of 37–42° with a counting time of 6 s to better reveal a possible beta phase.

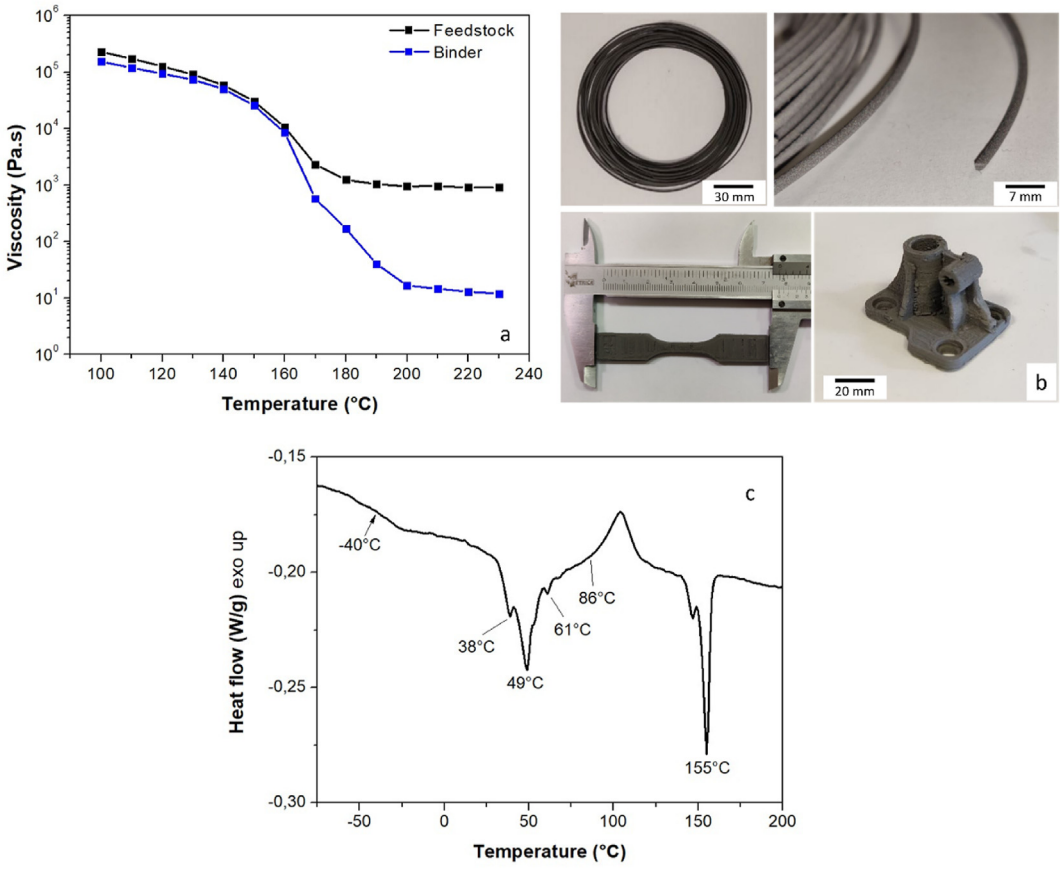

Fig. 4 – (a) Comparison of feedstock viscosity and binder viscosity as a function of temperature. (b) Extruded filaments and representative 3D printed samples, i.e., tensile test specimen and ribbed scaffolding base plate. (c) DSC of the feedstock.

at 60 °C) and mechanically polished using silicon carbide (SiC) papers and diamond suspension up to 3 μm, then ultrasonicated in a bath of ethanol.

A chemical etching consisting of a water solution (H_2O) of nitric acid (HNO_3, *Sigma Aldrich*) and hydrofluoric acid (HF, *Sigma Aldrich*) in the volume ratio H_2O: HNO_3: HF = 100 : 55: 5, was performed to reveal the grain boundaries. Both polished and etched surface morphologies have been imaged using optical microscopy (*Nikon Epiphot TME, Nikon Corporation, Tokyo, Japan*) coupled with an acquisition camera (*Visicam 10.0, VWR-Avantor, Radnor, Pennsylvania, USA*). Image analysis was performed by *ImageJ* software, allowing to calculate the grain size and the percentage of porosity. The grain size was evaluated according to ASTM E112-13 [43] using the intercept method and 200 measurements were made using different micrographs taken in different zones of the specimen. Electron microscopy (SEM, *Leo Supra Zeiss*) and EDS analysis were also performed.

Mechanical properties of sintered samples have been obtained performing tensile test according to ASTM E8/E8M [44] with a universal testing machine (*Instron 5569, Instron, Norwood, Massachusetts, USA*) setting a crosshead speed of 5 mm/min. Three specimens were tested.

The yield strength was calculated also with the Hall–Petch equation shown in Eq. (1):

$$\sigma_y = \sigma_0 + k_s / \sqrt{d} \quad (1)$$

where σ_y is the yield strength of polycrystalline metals, d the average grain size and σ_0 and k_s are constants for the metal, taken from literature, as 737 MPa and 230 MPa $\mu m^{1/2}$, respectively [45].

Vickers micro-hardness test (*Future Tech FM-700, Future Tech Corp., Kawasaki, Japan*), according to ASTM Standard E92 [46], was performed applying a load of 500 g for 30 s. Ten indentations were performed on the cross-section of mounted sintered sample.

Table 2 – Summary of the parameters used to 3D print the green parts.

Printing Parameters	Unit	Value
Nozzle diameter	mm	0.4
Nozzle Temperature	°C	250
Bed Temperature	°C	40
Layer thickness	mm	0.2
Infill	%	100
Raster angle (Rectilinear)	°	0–90
Perimeter lines	–	2
Printing Speed	mm/s	30

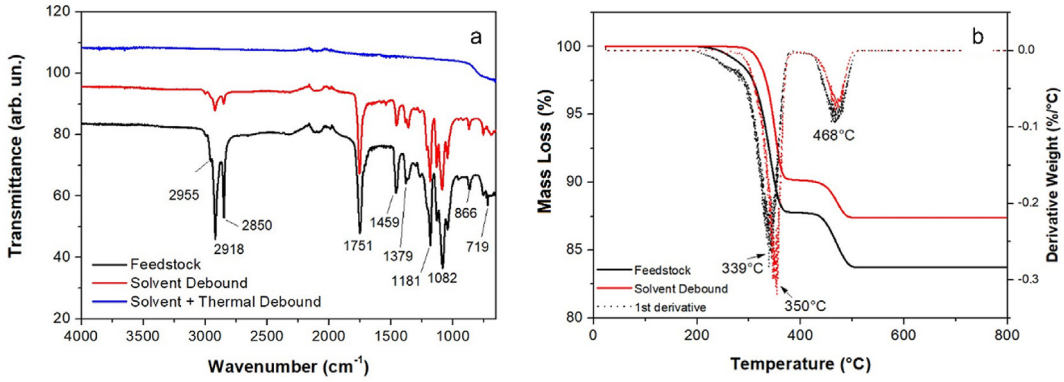

Fig. 5 – (a) FT-IR of 3D printed, solvent debound and thermally debound samples. (b) TGA and dTG thermograms of 3D printed and solvent debound samples.

3. Results and discussion

3.1. *Results of raw materials characterization*

The gas atomized titanium powder was fully characterized performing morphological, chemical composition, and microstructural analyses. SEM micrographs of the powder shown in Fig. 3a and b highlight a spherical morphology of the particles, with few inclusions of quasi-spherical ones and very few satellite particles ascribed to the gas atomization process.

The EDS analysis (Fig. 3c) highlights the typical composition of the as-received Ti6Al4V alloy, as the detected elements

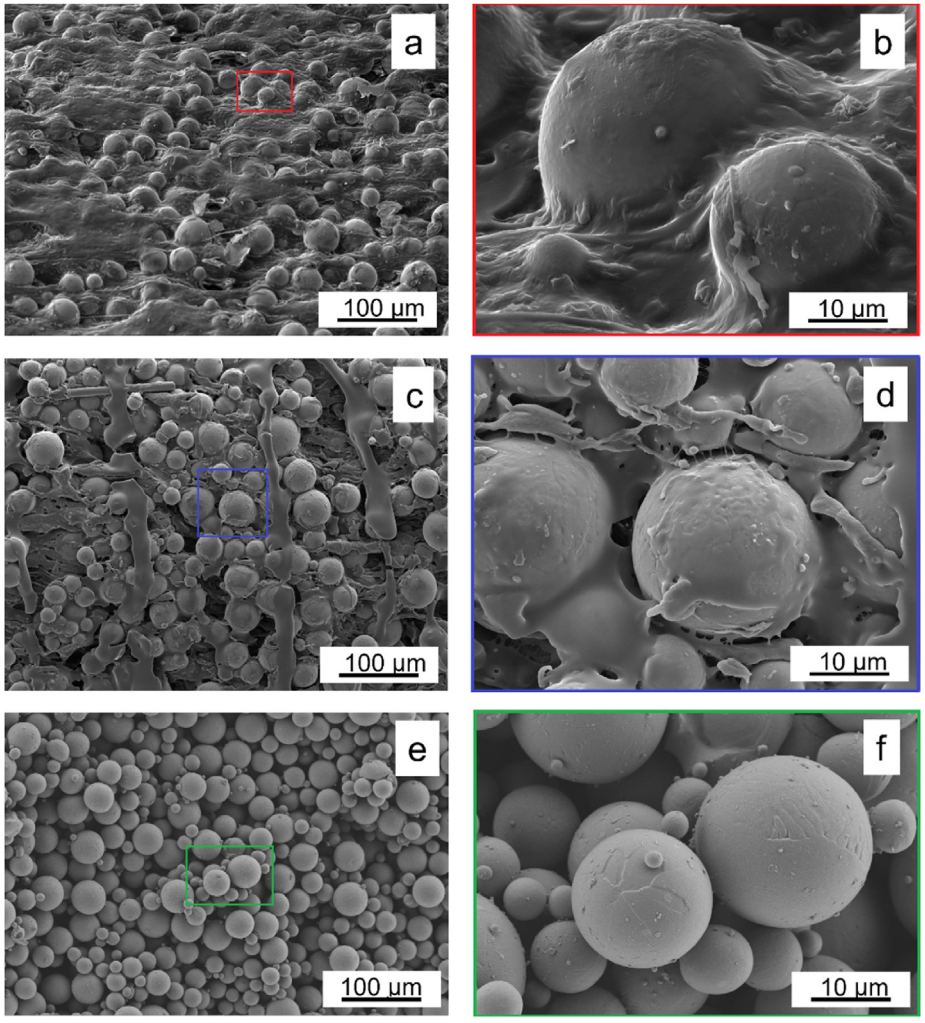

Fig. 6 – SEM morphology of (a–b) 3D printed sample, (c–d) solvent debound sample and (e–f) thermally debound sample.

Table 3 – Average dimension variation of 3D printed and sintered samples.

	3D printed (mm)	Sintered (mm)	Shrinkage (%)
Length	30.06	26.13	13.07
Width	20.03	17.31	13.57
Thickness	3.01	2.62	12.95

are Titanium, Aluminum and Vanadium. No presence of oxygen was revealed confirming the purity of the powders and the absence of oxidation phenomena. The measured particle distribution calculated on 40 different SEM micrographs is reported in Fig. 3d. The Ti6Al4V particles are characterized by an average diameter of 37 μm and most of them featured a diameter lower than 50 μm guaranteeing a good processability [18].

The X-ray diffraction pattern of the powder is displayed in Fig. 3e. The pattern shows diffraction peaks at $2\theta = 35.49°$, 38.67° 40.59°, 53.57° 63.91° 71.31 and 77.27° indicating a principal α Ti (hexagonal close-packed, hcp) phase corresponding to the reference pattern JCPDS 44–1294 without obvious peaks of the β Ti (body-centered cubic, bcc) phase.

3.2. *Feedstock rheology and 3D printing*

The feedstock viscosity is paramount to the extrusion of the material during the FFF printing. In particular, the filaments must act as a piston in the nozzle pushing the melted feedstock to create the continuous flow during extrusion [47], therefore the viscosity drop should be quite sharp in a small range of temperature. The viscosity measured by the rheological test of the developed feedstock in the range of 100–230 °C is shown in Fig. 4a and is compared to that of the neat binder. Viscosity values are very high (>10^5 Pa s) at 100 °C and present a drop in the temperature range 140–200 °C, which corresponds to the melting of the PLA confirmed also by the DSC analysis presented in Fig. 4c.

During heating the feedstock presents several endothermic peaks which, in accordance with the DSC performed on the single binder components, can be associated to the melting of the paraffin wax (38 °C and 49 °C), stearic acid (61 °C), EVA (86 °C) and PLA (155 °C), respectively. As expected, feedstock melt viscosity (Fig. 4a) is far higher than neat binder (1000 Pa s vs 10 Pa s at 230 °C) due to the filler–filler interactions. Nevertheless as clearly visible after 200 °C, viscosity remains quite stable and its value is in the range suitable for FFF printing, namely 10^2–10^5 Pa s [48,49], guaranteeing the proper rheological behavior of the melted feedstock.

In Fig. 4b the extruded filament, having average diameter of 1.68 ± 0.15 mm, and some representative 3D printed samples, with simple and complicated geometry, are shown. During printing, overflow and underflow issues were not recorded. The printed parts showed a good geometrical accuracy and no evidence of layer detachment or other macroscopic defects. In this perspective, the proposed bio-based binder appears to be a suitable choice to obtain a performing 3D printing filament while reducing the environmental impact of the feedstock.

3.3. *Solvent and thermal debinding: FT-IR and TGA results*

Fig. 5a reports the comparison of FT-IR spectra from the as 3D printed, the solvent debound and the solvent and thermally debound samples. The IR spectrum of 3D printed sample shows peaks which are representative of the different components of the binder.

In particular, the spectrum shows the peaks at 2955, 2918 and 2850 cm^{-1} that are ascribable to the CH_2 and CH_3 asymmetrical and symmetrical stretching, as well as the peaks at 1459 cm^{-1} and 719 cm^{-1} due to the CH_2 bending and wagging, mostly relative to paraffin wax [50,51], but also with the contribution of SA, EPDM, EVA and PLA. The sharp peak at 1751 cm^{-1} is related to the stretching of C=O bond relative to the PLA and EVA. Peak at 1379 cm^{-1}, the sharp peak at 1181 cm^{-1} (C–O stretching) as well as the trident peak centered at 1082 cm^{-1}, and the peak at 866 cm^{-1} are those typical of the finger prints of PLA [52], which is the constituent of the backbone binder. After solvent debinding, the peaks relative to the paraffin wax and stearic acid such as the stretching of methyl and methylene groups (triplets in the range 2955–2850 cm^{-1}) are strongly attenuated or completely disappeared such as the peak at 719 cm^{-1}.

This result confirms that the solvent debinding is effective in selectively removing the binder components and this conclusion is further corroborated by the thermogravimetric analysis presented in Fig. 5b. TGA performed on 3D printed sample shows that the binder has a two-step degradation process, the first one at 339 °C which is mainly due to thermal degradation of PLA which from literature is known to degrade in the range 300–400 °C by chain scission where the PLA chains break apart

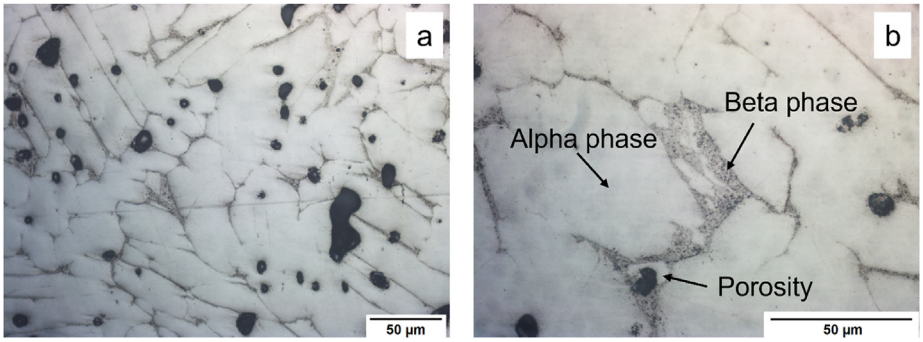

Fig. 7 – Optical microscopy at (a) 200X and (b) 400X of polished 3D printed sintered sample.

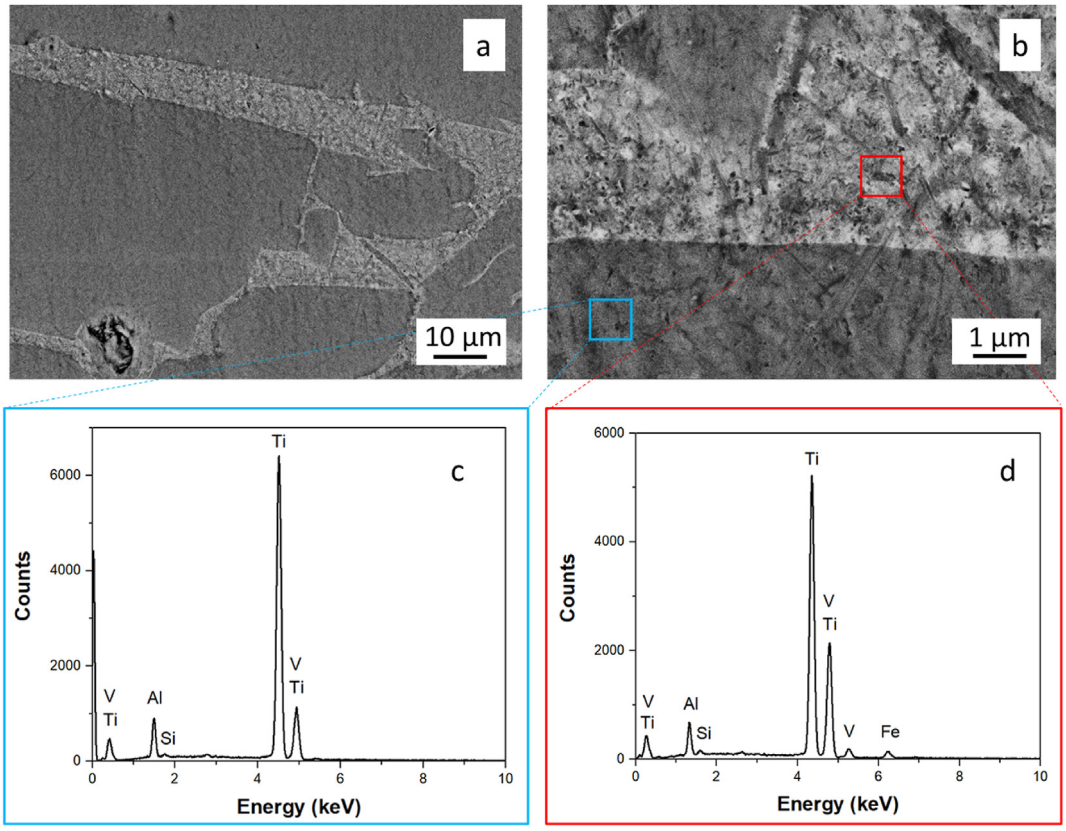

Fig. 8 – (a, b) SEM micrographs of sintered Ti6Al4V sample and EDS spectrum of (c) alpha and (d) beta phase.

due to the cleavage of ester bonds [53]. The second degradation is at 468 °C and it is relative to the thermal scission of the other binder components in particular PW and EPDM [54]. The residue at 800 °C for the 3D printed sample confirmed the composition of the feedstock with 83.8 wt.% of titanium particles and 16.2 wt.% of binder. The solvent debound sample was also tested by TGA. The solvent is effective in removing the paraffin wax and the stearic acid as confirmed by the difference in the residue at 800 °C which is equal to a 20% of binder removal corresponding to the sum of the PW and SA (15 wt.% and 5 wt.% of the binder) content. From TGA is evident that the thermal degradation ends at 500 °C, hence the temperature for the debinding was set at 600 °C to ensure the complete binder removal.

The SEM analysis performed on 3D printed, solvent debound and thermally debound samples is presented in Fig. 6. Fig. 6a and b show the 3D printed sample and highlight a good dispersion of the metallic particles that are covered by a thin layer of binder.

Table 4 – Composition of the alpha and beta grains of 3D printed sample from EDS analysis.

Element	Alpha phase wt.%	Beta Phase wt.%
Ti	Balance	Balance
Al	5.36	4.64
V	3.69	22.54
Fe	–	3.16

During solvent debinding, the solvent chemically dissolves part of the binder exposing the outer particles and creating the porosities shown in Fig. 6c and d. This ensures the correct elimination of the volatile compounds which form during the subsequent thermal decomposition of the binder.

After the thermal treatment, the binder appears completely removed in accordance with the FT-IR analysis performed on the thermally debound sample (Fig. 5a) and the metallic particles are in contact with each other (Fig. 6e and f). This is a crucial aspect for a successful sintering process since during the first sintering stage necking formation between two adjacent particles takes place. During sintering, the applied heat causes the atom vibration increasing their mobility. According to the mass transport mechanisms, i.e., evaporation and condensation, surface diffusion, and volume diffusion [55], atoms of the material can easily move between the surface contact of the particles determining the formation of the neck between the two particles which successively grows [56]. If binder residues were present during the initial stages of sintering, the defects such as cracking and bloating could be formed as a result of the stress applied by the trapped gas originating by the binder decomposition. The chemical composition of the binder, in particular both the carbon and the oxygen content in the repeating unit of the backbone binder, is a critical factor in determining the success of the debinding process. Carbon content plays a strong impact on the volatile by-production, the residue formation and consequently on the shrinkage and distortion [57] affecting also the mechanical properties [58]. On the other hand, the presence of

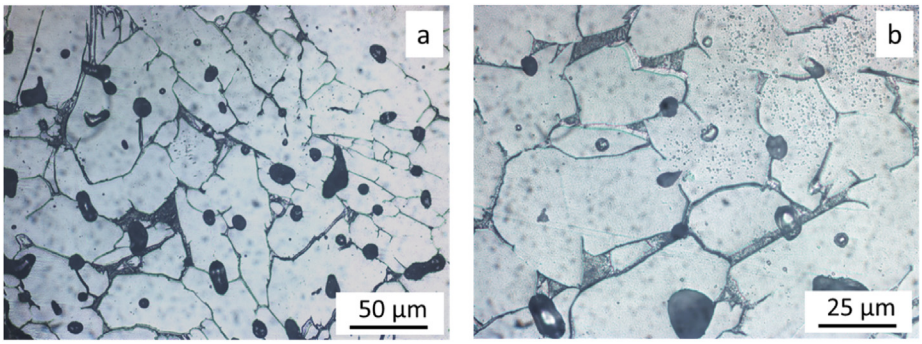

Fig. 9 – Optical microscopy at (a) 200X and (b) 400X of 3D printed sintered sample after chemical etching highlighting grain boundaries.

oxygen can lead to the formation of metal oxides or hydroxides during the sintering process [59].

3.4. *Characterization of 3D printed sintered samples*

The sintered samples have been measured and shrinkage along X, Y and Z direction was assessed. The related results are reported in Table 3. As expected, samples present a reduction of about 13% in the dimensions as the result of the elimination of pores in the green body due to the bulk transport mechanisms such as plastic flow, viscous flow, grain boundary diffusion, and volume diffusion. This value complies with the Typical MIM shrinkage which is within the range of 12–20% [13].

The measured mean density value is 4.17 ± 0.15 g/cm^3 and it corresponds to a 5.8% of porosity considering the theoretical density of Ti6Al4V alloy (4.43 g/cm^3) [60]. These results are coherent with the ones reported by Singh et al. [61] who reported a 5.8% of porosity with a 14% of shrinkage and with the ones reported by Nor et al. [62] who observed a lower density, i.e., a higher porosity, of 4.03 g/cm^3, for a lower shrinkage of 10.55–11%.

This value has been confirmed by the image analysis performed on the polished cross section surface of the sample. From image analysis (Fig. 7a) emerges the presence of some intergranular round porosity.

The presence of porosity in specimens manufactured by FFF is an intrinsic drawback, but the shape and type of porosities can provide information on the cause determining it [63]. If the porosity is spherical, as in the present work, it is generally connected to thermal treatment of debinding [64]. According to these results, the densification after sintering is in the range of 94–95% which is comparable to the densification obtained with Metal Injection Molding (MIM) process [65]. From the micrographs, it is also possible to appreciate the presence of both alpha and beta phases.

Fig. 7a and b show a α (light grey) major phase and an intergranular (dark grey) β phase. This microstructure is known as beta segregation and it was confirmed by the SEM-BSE and the EDS analysis, shown in Fig. 8 and Table 4, respectively, which reports the alloy phases' compositions. The SEM micrographs, acquired with backscattered detector, show a α (dark grey) grains with segregated intergranular (light grey) vanadium rich β phase due to the fact that vanadium has high relative atomic mass (50.94 u).

Moreover, the EDS analysis highlights a different composition of the two phases with the alpha phase displaying the typical composition of Ti6Al4V alloy with aluminum content of 5.36% and vanadium 3.69%, in accordance with the datasheet of the powder, and the beta phase displaying a high content of vanadium 22.54% and iron 3.16%. V and Fe atoms are strong β-stabilizing elements [66,67] and the atomic ratio

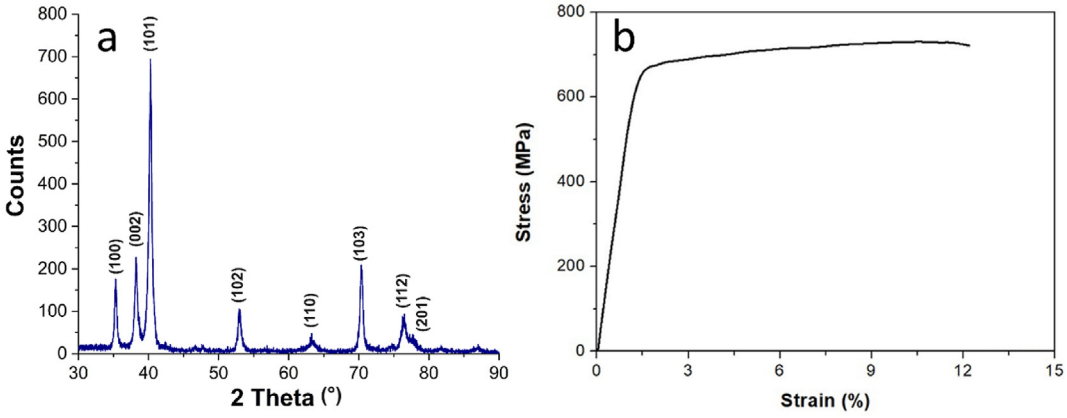

Fig. 10 – (a) XRD pattern of sintered sample and (b) representative stress–strain curve of 3D printed sintered Ti6Al4V sample.

Table 5 – Mechanical properties of sintered 3D printed samples.

σ_y (MPa)	UTS (MPa)	ε_{max} (%)
662.4 ± 12.2	742.6 ± 14.1	12.3 ± 1.3

of these elements is higher in the β phase than that in the α phase because of the higher solid solubility and elemental diffusion rate in the β phase [68]. The EDS spectra do not show oxygen and carbon presence thus proving the good control on both debinding and sintering processes. Carbon content is a contaminant coming from the organic binder and the final carbon concentration has to be kept below 0.08 wt.% in order to avoid the formation of Titanium carbide [69]. These results confirm that PLA can be effectively used as biobased backbone binder. Small traces of silicon were detected in both alpha and beta phases by the EDS analysis and can be likely ascribed to the mechanical polishing phase which was performed with SiC papers.

In Fig. 9a and b the microstructure of the sintered sample after the chemical etching evidencing the grain boundaries is reported. The grains have an equiaxial structure with a mean grain size, calculated by the intercept method, of 70 ± 3 μm.

Fig. 10a reports the XRD pattern of the sintered sample and compared with the reference patterns of both α-hexagonal and β-body-centered cubic Ti, the main phase is found to be αTi, which is coherent with its low content and to its strong localization at the grain boundaries as evidenced by SEM, which make the overall diffraction pattern dominated by the alpha phase.

The absence of diffraction peaks related to carbides and oxides confirms the good control on both debinding and sintering processes and corroborates the feasibility of the proposed bio-based polymer blend as filament binder.

In Fig. 10b, a representative tensile curve of the 3D printed Ti6Al4V alloy is displayed and in Table 5 the main mechanical properties are reported.

The mechanical properties obtained are comparable with other works where FFF of Titanium alloys have been performed but are, as expected, lower than Ti6Al4V alloys produced by traditional techniques [70,71]. In particular, the tensile strength obtained is significantly lower than the 850 [72] – 1032 MPa [73] achievable with EBM, than the 1080 [74] – 1421 MPa [75] achievable with SLM and than the 1025 [76] –1097 MPa [77] achievable with Direct Energy Deposition (DED) thus highlighting the need to optimize the 3D printing parameters to fill this gap as much as possible. At the same time, the tensile strength is somewhat comparable with MIM components characterized by values between 704 [78] and 934 MPa [79]. Moreover, Thompson et al. [15] reported a 350 MPa tensile strength for components produced by BMD which is significantly lower than the one obtained in the present work.

The calculated yield strength of the sintered 3D printed sample, by applying the Hall–Petch's equation, resulted to be 764.5 MPa which is higher than the one obtained from the tensile test but the presence of porosity might have reduced the mechanical properties.

Microhardness test has shown a mean hardness value of 526.6 HV which is equivalent to 5.15 GPa and is coherent with the hardness values of Ti6Al4V alloys which generally ranges from 350 to 570 HV [80], depending on the relative proportion of α and β phases. Moreover, authors reported that the hardness of titanium alloy increases with increasing the sintering temperature [78]. In the present work, the high sintering temperature and the high amount of α phase, hard and brittle [81], justifies the high global hardness value.

4. Conclusions

In this paper polylactic acid (PLA) was employed as a biobased backbone binder for the production of Ti6Al4V feedstock, which has been extruded in filaments and then 3D printed via fused filament fabrication and successively debound and sintered to obtain a fully dense metallic part.

The binder presents a good rheological behavior and, when loaded with the metallic filler, the feedstock has viscosity values suitable for FFF process already in the temperature range 140–200 °C.

The solvent and the thermal debinding allow to remove all the organic binder components without generating cracks or other visible defects. Sintering in reducing atmosphere ($Ar–H_2$) leads to a densified metallic component having a degree of porosity of 5.8% perfectly comparable with parts produced via metal injection molding and with a microstructure composed of primary grains of alpha phase with beta phase segregated at the grain boundaries.

Sintered samples show good mechanical properties, i.e., σ_y = 662.4 ± 12.2 MPa, UTS = 742.6 ± 14.1 MPa and ε_{max} = 12.3 ± 1.3%, comparable with the ones of other works where Ti6Al4V was manufactured by BMD. Moreover, the chemical composition free of carbon and oxygen contamination further confirms that PLA is a suitable candidate as backbone binder in view of a more sustainable process.

Funding

This work was supported by the Regione Lazio, "Progetti di Gruppi di Ricerca 2020" – POR FESR LAZIO 2014–2020, Project A0375E0191, CUP E85F21002410002, 3D printing di strutture metalliche aerospaziali da feedstock polimerici (3D-PolMet).

Declaration of Competing Interest

The authors declare that they have no known competing financial interests or personal relationships that could have appeared to influence the work reported in this paper.

REFERENCES

[1] Rajan KM, Sahoo AK, Routara BC, Panda A, Kumar R. A review on various approaches of 3D printing of Ti-Alloy.

Mater Today Proc 2022;62:3865–8. https://doi.org/10.1016/j.matpr.2022.04.532.
[2] Zhang T, Liu CT. Design of titanium alloys by additive manufacturing: a critical review. Adv Powder Mater 2022;1:100014. https://doi.org/10.1016/j.apmate.2021.11.001.
[3] Leary M. Design for additive manufactruing. Amsterdam: Elsevier Inc.; 2019.
[4] Taufek T, Adenan MS, Manurung YHP, Sulaiman SA, Zaid NS, Romzi NAS. 3D metal printing using generative design and numerical computation. Recent trends manuf. Mater. Towar. Ind.. Singapore: Springer Nature Singapore; 2021. p. 839–49. 4.0.
[5] Ren L, Zhou X, Song Z, Zhao C, Liu Q, Xue J, et al. Process parameter optimization of extrusion-based 3D metal printing utilizing PW-LDPE-SA binder system. Materials 2017;10:305–29. https://doi.org/10.3390/ma10030305.
[6] Gong H, Snelling D, Kardel K, Carrano A. Comparison of stainless steel 316L parts made by FDM- and SLM-based additive manufacturing processes. JOM (J Occup Med) 2019;71:880–5. https://doi.org/10.1007/s11837-018-3207-3.
[7] Formlabs. 3D Printing Technology Comparison: FDM vs. SLA vs. SLS 2023. https://formlabs.com/blog/fdm-vs-sla-vs-sls-how-to-choose-the-right-3d-printing-technology/(accessed July 4, 2023).
[8] Markforged. Types of 3D Printing in Metal 2023. https://markforged.com/resources/learn/design-for-additive-manufacturing-metals/metal-additive-manufacturing-introduction/types-of-3d-printing-metal?__geom=✪ (accessed July 18, 2023).
[9] Ziaee M, Crane NB. Binder jetting: a review of process, materials, and methods. Addit Manuf 2019;28:781–801. https://doi.org/10.1016/j.addma.2019.05.031.
[10] Mostafaei A, Elliott AM, Barnes JE, Li F, Tan W, Cramer CL, et al. Binder jet 3D printing—process parameters, materials, properties, modeling, and challenges. Prog Mater Sci 2021;119:100707. https://doi.org/10.1016/j.pmatsci.2020.100707.
[11] Cavallo C. All about binder jetting 3D printing 2023. https://www.thomasnet.com/articles/custom-manufacturing-fabricating/all-about-binder-jetting-3d-printing/(accessed September 15, 2023).
[12] Pick3DPrinter. Best binder jetting 3D printer – pros and cons & buying guide 2023. 2023. https://pick3dprinter.com/binder-jetting-3d-printer/. [Accessed 15 September 2023].
[13] Suwanpreecha C, Manonukul A. A review on material extrusion additive manufacturing of metal and how it compares with metal injection moulding. Metals 2022;12:429. https://doi.org/10.3390/met12030429.
[14] Sadaf M, Cano S, Gonzalez-Gutierrez J, Bragaglia M, Schuschnigg S, Kukla C, et al. Influence of binder composition and material extrusion (MEX) parameters on the 3D printing of highly filled copper feedstocks. Polymers 2022;14:4962. https://doi.org/10.3390/polym14224962.
[15] Thompson Y, Polzer M, Gonzalez-Gutierrez J, Kasian O, Heckl JP, Dalbauer V, et al. Fused filament fabrication-based additive manufacturing of commercially pure titanium. Adv Eng Mater 2021;23:2100380. https://doi.org/10.1002/adem.202100380.
[16] Shaikh MQ, Lavertu P-Y, Kate KH, Atre SV. Process sensitivity and significant parameters investigation in metal fused filament fabrication of Ti-6Al-4V. J Mater Eng Perform 2021;30:5118–34. https://doi.org/10.1007/s11665-021-05666-8.
[17] Zhang Y, Bai S, Riede M, Garratt E, Roch A. A comprehensive study on fused filament fabrication of Ti-6Al-4V structures. Addit Manuf 2020;34:101256. https://doi.org/10.1016/j.addma.2020.101256.
[18] Singh P, Balla VK, Atre SV, German RM, Kate KH. Factors affecting properties of Ti-6Al-4V alloy additive manufactured by metal fused filament fabrication. Powder Technol 2021;386:9–19. https://doi.org/10.1016/j.powtec.2021.03.026.
[19] Shaikh MQ, Graziosi S, Atre SV. Supportless printing of lattice structures by metal fused filament fabrication (MF 3) of Ti-6Al-4V: design and analysis. Rapid Prototyp J 2021;27:1408–22. https://doi.org/10.1108/RPJ-01-2021-0015.
[20] Bek M, Gonzalez-Gutierrez J, Kukla C, Črešnar KP, Maroh B, Perše LS. Rheological behaviour of highly filled materials for injection moulding and additive manufacturing: effect of particle material and loading. Appl Sci 2020;10:1–23. https://doi.org/10.3390/app10227993.
[21] Gonzalez-Gutierrez J, Cano S, Schuschnigg S, Kukla C, Sapkota J, Holzer C. Additive manufacturing of metallic and ceramic components by the material extrusion of highly-filled polymers: a review and future perspectives. Materials 2018;840. https://doi.org/10.3390/ma11050840.
[22] Riecker S, Hein S, Studnitzky T, Andersen O, Kieback B. 3D printing of metal parts by means of fused filament fabrication-A non beam-based approach 3D printing of metal parts by means of fused filament fabrication - a non beam-based approach. Int. Powder Metall. Congr. Exhib. Euro PM2017 – AM Altern. Technol. 2017.
[23] Singh P, Balla VK, Tofangchi A, Atre SV, Kate KH. Printability studies of Ti-6Al-4V by metal fused filament fabrication (MF3). Int J Refract Met Hard Mater 2020;91:105249. https://doi.org/10.1016/j.ijrmhm.2020.105249.
[24] Venkataraman N, Rangarajan S, Matthewson MJ, Safari A, Danforth SC, Yardimci A. Mechanical and rheological properties of feedstock material for fused deposition of ceramics and metals (FDC and FDMet) and their relationship to process performance. Solid Free. Fabr. Proc. 1999:351–9.
[25] Kukla C, Gonzalez-gutierrez J, Duretek I, Schuschnigg S, Holzer C. Effect of particle size on the properties of highly-filled polymers for fused filament fabrication. AIP Conf. Proceedings, 32nd Int. Conf. Polym. Process. Soc. - Conf. Pap. 2017;1914. https://doi.org/10.1063/1.5016795.
[26] Brostow W, Buchman A, Buchman E, Olea-mejia O. Microhybrids of metal powder incorporated in polymeric matrices : friction , mechanical behavior , and microstructure. 2008. p. 1–5. https://doi.org/10.1002/pen.
[27] Uhm YR, Kim J, Son KJ, Kim CS. Effect of particle size, dispersion, and particle–matrix adhesion on W reinforced polymer composites. Res Chem Intermed 2014;40:2145–53. https://doi.org/10.1007/s11164-013-1110-7.
[28] Gonzalez-Gutierrez J, Duretek I, Kukla C, Poljšak A, Bek M, Emri I, et al. Models to predict the viscosity of metal injection molding feedstock materials as function of their formulation. Metals 2016;6. https://doi.org/10.3390/met6060129.
[29] Gonzlez-Gutirrez J, Stringari GB, Emri I. Powder injection molding of metal and ceramic parts. Some crit. Issues inject. Molding. London: IntechOpen; 2012. p. 65–88. https://doi.org/10.5772/38070.
[30] Kukla C, Gonzalez-gutierrez J, Felfer P, Holzer, Clemens, Schuschnigg, et al. Material extrusion with filaments for the production of metal parts and feedstock therefore. Met. Addit. Manuf. Conf. 2018.
[31] Md Ani S, Muchtar A, Muhamad N, Ghani JA. Binder removal via a two-stage debinding process for ceramic injection molding parts. Ceram Int 2014;40:2819–24. https://doi.org/10.1016/j.ceramint.2013.10.032.
[32] Kong X. Development and characterization of polymer-metallic powder feedstocks for micro-injection molding. 2011.
[33] Eickhoff R, Antusch S, Baumgärtner S, Nötzel D, Hanemann T. Feedstock development for material extrusion-based printing of Ti6Al4V parts. Materials 2022;15:6442. https://doi.org/10.3390/ma15186442.

[34] Taib N-AAB, Rahman MR, Huda D, Kuok KK, Hamdan S, Bakri MK Bin, et al. A review on poly lactic acid (PLA) as a biodegradable polymer. Polym Bull 2023;80:1179–213. https://doi.org/10.1007/s00289-022-04160-y.
[35] Trivedi AK, Gupta MK, Singh H. PLA based biocomposites for sustainable products: a review. Adv Ind Eng Polym Res 2023;6:382–95. https://doi.org/10.1016/j.aiepr.2023.02.002.
[36] Moretti C, Hamelin L, Jakobsen LG, Junginger MH, Steingrimsdottir MM, Høibye L, et al. Cradle-to-grave life cycle assessment of single-use cups made from PLA, PP and PET. Resour Conserv Recycl 2021;169:105508. https://doi.org/10.1016/j.resconrec.2021.105508.
[37] DebRoy T, Wei HL, Zuback JS, Mukherjee T, Elmer JW, Jo Milewski, et al. Additive manufacturing of metallic components – process, structure and properties. Prog Mater Sci 2018;92:112–224. https://doi.org/10.1016/J.PMATSCI.2017.10.001.
[38] Mirzababaei S, Pasebani S. A review on binder jet additive manufacturing of 316L stainless steel. J Manuf Mater Process 2019;3. https://doi.org/10.3390/jmmp3030082.
[39] Tosto C, Tirillò J, Sarasini F, Sergi C, Cicala G. Fused deposition modeling parameter optimization for cost-effective metal Part Printing. Polymers 2022;14:1–22. https://doi.org/10.3390/polym14163264.
[40] Heaney Donald F, editor. Handbook of metal injection molding. Sawston: Woodhead Publishing; 2012.
[41] American Society for Testing and Materials. Astm D638: standard test method for tensile properties of plastics, 8. B. ASTM Stand.; 2022. p. 17. https://doi.org/10.1520/D0638-14.01.
[42] American Society for Testing and Materials. Astm D792: standard test methods for density and specific gravity (relative density) of plastics by displacement, 8. B. ASTM Stand.; 2020. p. 6. https://doi.org/10.1520/D0792-20. 01.
[43] American Society for Testing and Materials. Astm E112: standard test methods for determining average grain size, 3. B. ASTM Stand.; 2013. p. 28. https://doi.org/10.1520/E0112-13R21. 01.
[44] American Society for Testing and Materials. Astm E8/E8M: standard test methods for tension testing of metallic materials. B. ASTM Stand.; 2022. p. 31. https://doi.org/10.1520/E0008_E0008M-22.
[45] Chong Y, Deng G, Gao S, Yi J, Shibata A, Tsuji N. Yielding nature and Hall-Petch relationships in Ti-6Al-4V alloy with fully equiaxed and bimodal microstructures. Scripta Mater 2019;172:77–82. https://doi.org/10.1016/j.scriptamat.2019.07.015.
[46] American Society for Testing and Materials. Astm E92: standard test methods for vickers hardness of matallic materials. B. ASTM Stand.; 2017. p. 27. https://doi.org/10.1520/E0092-17.
[47] Cano S, Gonzalez-Gutierrez J, Sapkota J, Spoerk M, Arbeiter F, Schuschnigg S, et al. Additive manufacturing of zirconia parts by fused filament fabrication and solvent debinding: selection of binder formulation. Addit Manuf 2019;26:117–28. https://doi.org/10.1016/j.addma.2019.01.001.
[48] Gibson MA, Mykulowycz NM, Shim J, Fontana R, Schmitt P, Roberts A, et al. 3D printing metals like thermoplastics: fused filament fabrication of metallic glasses. Mater Today 2018;21:697–702. https://doi.org/10.1016/j.mattod.2018.07.001.
[49] Khaliq H, Nobrega JM, Carneiro OS. On the use of high viscosity polymers in the fused filament fabrication process. Rapid Prototyp J 2017;23:727–35. https://doi.org/10.1108/RPJ-02-2016-0027.
[50] Khanifah L, Widodo S, Widarto, Putra NMD, Satrio A. Characteristics of paraffin shielding of kartini reactor, yogyakarta. ASEAN J Sci Technol Dev 2018;35:195–8. https://doi.org/10.29037/ajstd.526.
[51] Kumar K, Sharma K, Verma S, Upadhyay N. Experimental investigation of graphene-paraffin wax nanocomposites for thermal energy storage. Mater Today Proc 2019;18:5158–63. https://doi.org/10.1016/j.matpr.2019.07.513.
[52] Singla P, Mehta R, Berek D, Upadhyay SN. Microwave assisted synthesis of poly(lactic acid) and its characterization using size exclusion chromatography. J Macromol Sci Part A 2012;49:963–70. https://doi.org/10.1080/10601325.2012.722858.
[53] Kervran M, Vagner C, Cochez M, Ponçot M, Saeb MR, Vahabi H. Thermal degradation of polylactic acid (PLA)/polyhydroxybutyrate (PHB) blends: a systematic review. Polym Degrad Stabil 2022;201:109995. https://doi.org/10.1016/j.polymdegradstab.2022.109995.
[54] Bragaglia M, McNally T, Lamastra FR, Cherubini V, Nanni F. Compatibilization of an immiscible blend of EPDM and POM with an Ionomer. J Appl Polym Sci 2021;138:1–16. https://doi.org/10.1002/app.50423.
[55] Sadaf M, Bragaglia M, Nanni F. A simple route for additive manufacturing of 316L stainless steel via Fused Filament Fabrication. J Manuf Process 2021;67:141–50. https://doi.org/10.1016/j.jmapro.2021.04.055.
[56] Banerjee S, Joens CJ. Debinding and sintering of metal injection molding (MIM) components. Handb. Met. Inject. Molding. Sawston: Woodhead Publishing; 2012. p. 133–80. https://doi.org/10.1533/9780857096234.1.133.
[57] Herranz G. Control of carbon content in metal injection molding (MIM). Handb. Met. Inject. Molding. Sawston: Woodhead Publishing; 2012. p. 265–304. https://doi.org/10.1533/9780857096234.2.265.
[58] Obasi GC, Ferri OM, Ebel T, Bormann R. Influence of processing parameters on mechanical properties of Ti–6Al–4V alloy fabricated by MIM. Mater Sci Eng, A 2010;527:3929–35. https://doi.org/10.1016/j.msea.2010.02.070.
[59] Wen G, Cao P, Gabbitas B, Zhang D, Edmonds N. Development and design of binder systems for titanium metal injection molding: an overview. Metall Mater Trans A 2013;44:1530–47. https://doi.org/10.1007/s11661-012-1485-x.
[60] Lin Y, Shi W, Li J, Liu Y, Liu S, Li J. Evaluation of mechanical properties of Ti–6Al–4V BCC lattice structure with different density gradient variations prepared by L-PBF. Mater Sci Eng, A 2023;872:144986. https://doi.org/10.1016/j.msea.2023.144986.
[61] Singh P, Balla VK, Atre SV, German RM, Kate KH. Factors affecting properties of Ti-6Al-4V alloy additive manufactured by metal fused filament fabrication. Powder Technol 2021;386:9–19. https://doi.org/10.1016/j.powtec.2021.03.026.
[62] Mohamad Nor NH, Ismail MH, Husain H, Saedon JB, Newishy M. Sintered strength of Ti-6Al-4V by metal injection molding (MIM) using palm stearin binder. J Mech Eng 2019;16:135–47. https://doi.org/10.24191/jmeche.v16i1.6044.
[63] Pigliaru L, Paleari L, Bragaglia M, Nanni F, Ghidini T, Rinaldi M. Poly-ether-ether-ketone – neodymium-iron-boron bonded permanent magnets via fused filament fabrication. Synth Met 2021;279:116857. https://doi.org/10.1016/j.synthmet.2021.116857.
[64] Sames WJ, List FA, Pannala S, Dehoff RR, Babu SS. The metallurgy and processing science of metal additive manufacturing. Int Mater Rev 2016;61:315–60. https://doi.org/10.1080/09506608.2015.1116649.
[65] Ahmad MA, Jabir M, Johari N, Ibrahim R, Hamidi N. The effect of impurities elements on titanium alloy (Ti-6Al-4V) MIM sintered part properties. AIP Conf Proceedings, Adv Mater Sustain GROWTH Proc 3rd Adv Mater Conf 2017;1901:040007. https://doi.org/10.1063/1.5010496. 2016 (3rd AMC 2016).
[66] Huang S, Ma Y, Zhang S, Qi M, Lei J, Zong Y, et al. Influence of alloying elements partitioning behaviors on the microstructure and mechanical properties in α+β titanium

alloy. Jinshu Xuebao/Acta Metall Sin 2019;55:741–50. https://doi.org/10.11900/0412.1961.2018.00460.
[67] Qiao Y, Xu D, Wang S, Ma Y, Chen J, Wang Y, et al. Corrosion and tensile behaviors of Ti-4Al-2V-1Mo-1Fe and Ti-6Al-4V titanium alloys. Metals 2019;9:1213. https://doi.org/10.3390/met9111213.
[68] Huang S, Zhang J, Ma Y, Zhang S, Youssef SS, Qi M, et al. Influence of thermal treatment on element partitioning in α+β titanium alloy. J Alloys Compd 2019;791:575–85. https://doi.org/10.1016/j.jallcom.2019.03.332.
[69] Fang ZZ, Paramore JD, Sun P, Chandran KSR, Zhang Y, Xia Y, et al. Powder metallurgy of titanium – past, present, and future. Int Mater Rev 2018;63:407–59. https://doi.org/10.1080/09506608.2017.1366003.
[70] Nguyen HD, Pramanik A, Basak AK, Dong Y, Prakash C, Debnath S, et al. A critical review on additive manufacturing of Ti-6Al-4V alloy: microstructure and mechanical properties. J Mater Res Technol 2022;18:4641–61. https://doi.org/10.1016/j.jmrt.2022.04.055.
[71] Singh P, Balla VK, Gokce A, Atre SV, Kate KH. Additive manufacturing of Ti-6Al-4V alloy by metal fused filament fabrication (MF3): producing parts comparable to that of metanjection molding. Prog Addit Manuf 2021;6:593–606. https://doi.org/10.1007/s40964-021-00167-5.
[72] Edwards P, O'Conner A, Ramulu M. Electron beam additive manufacturing of titanium components: properties and performance. J Manuf Sci Eng 2013;135:1–7. https://doi.org/10.1115/1.4025773.
[73] Chastand V, Quaegebeur P, Maia W, Charkaluk E. Comparative study of fatigue properties of Ti-6Al-4V specimens built by electron beam melting (EBM) and selective laser melting (SLM). Mater Char 2018;143:76–81. https://doi.org/10.1016/j.matchar.2018.03.028.
[74] Leuders S, Thöne M, Riemer A, Niendorf T, Tröster T, Richard HA, et al. On the mechanical behaviour of titanium alloy TiAl6V4 manufactured by selective laser melting: fatigue resistance and crack growth performance. Int J Fatig 2013;48:300–7. https://doi.org/10.1016/j.ijfatigue.2012.11.011.
[75] Wysocki B, Maj P, Sitek R, Buhagiar J, Kurzydłowski KJ, Świeszkowski W. Laser and electron beam additive manufacturing methods of fabricating titanium bone implants. Appl Sci 2017;7. https://doi.org/10.3390/app7070657.
[76] Qiu C, Ravi GA, Dance C, Ranson A, Dilworth S, Attallah MM. Fabrication of large Ti-6Al-4V structures by direct laser deposition. J Alloys Compd 2015;629:351–61. https://doi.org/10.1016/j.jallcom.2014.12.234.
[77] Sterling AJ, Torries B, Shamsaei N, Thompson SM, Seely DW. Fatigue behavior and failure mechanisms of direct laser deposited Ti-6Al-4V. Mater Sci Eng, A 2016;655:100–12. https://doi.org/10.1016/j.msea.2015.12.026.
[78] Ergül E, Özkan Gülsoy H, Günay V. Effect of sintering parameters on mechanical properties of injection moulded Ti–6Al–4V alloys. Powder Metall 2009;52:65–71. https://doi.org/10.1179/174329008X271691.
[79] Nor NHM, Muhamad N, Ihsan AKAM, Jamaludin KR. Sintering parameter optimization of Ti-6Al-4V metal injection molding for highest strength using palm stearin binder. Procedia Eng 2013;68:359–64. https://doi.org/10.1016/j.proeng.2013.12.192.
[80] Kaouka A, Benarous K, Daas A, Tsipas SA. The effects of Nb and Mo addition on microstructure and mechanical behaviour of Ti-6Al-4V alloy. J Surf Sci Technol 2017;33:53. https://doi.org/10.18311/jsst/2017/11026.
[81] Bian T, Ding C, Yao X, Wang J, Mo W, Wang Z, et al. Mechanisms of heat treatment and ductility improvement of high-oxygen Ti–6Al–4V alloy fabricated by metal injection molding. Mater Sci Eng, A 2022;840:142924. https://doi.org/10.1016/j.msea.2022.142924.